INORGANIC CHEMISTRY

FRONTIERS

Accepted Manuscript

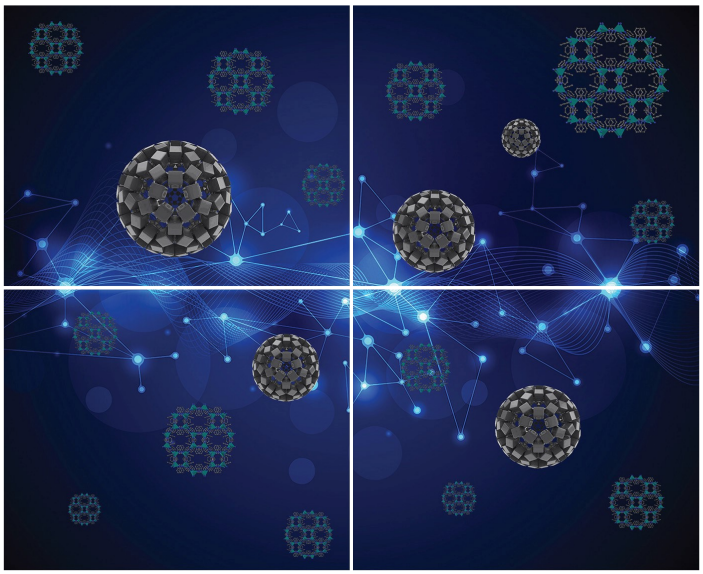

This article can be cited before page numbers have been issued, to do this please use: K. Lee, E. J. Lee, H. Lim and J. E. Lee, *Inorg. Chem. Front.*, 2026, DOI: 10.1039/D6QI00145A.

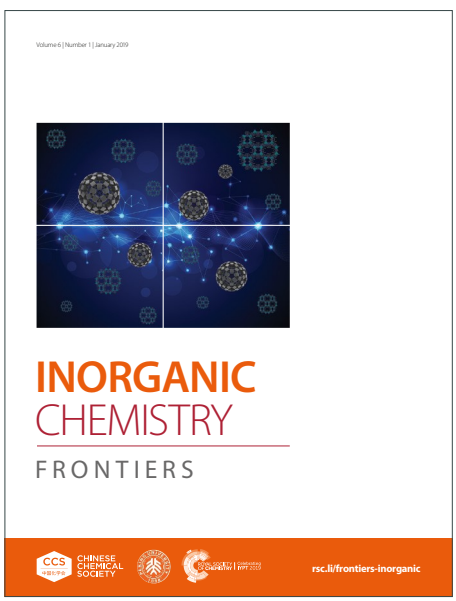

View Article Online
DOI: 10.1039/D6QI00145A

Ammonium Vanadium Oxide Nanobelt-Integrated Sulfur Hosts Enabling Enhanced Polysulfide Redox Kinetics in Lithium–Sulfur Batteries

Kiseok Lee,†[a] Eun Ji Lee,†[a] Hyung-Kyu Lim,*[b] Ji Eun Lee*[a]

[a]*Department of Chemical Engineering, Chonnam National University, Gwangju 61186, Republic of Korea. E-mail: jelee@jnu.ac.kr*

[b]*Department of Chemical Engineering and Bioengineering, Kangwon National University, Chuncheon 24341, Republic of Korea. E-mail: hklim@kangwon.ac.kr*

†These authors contributed equally.

Abstract

Lithium–sulfur (Li–S) batteries are regarded as promising next-generation energy storage systems, but their practical application is limited by the intrinsic insulating nature of sulfur, the dissolution and shuttling of lithium polysulfides, and sluggish redox kinetics. To address these challenges, a multifunctional sulfur host was developed by integrating biomass-derived activated carbon (AC) with ammonium vanadium oxide (NVO) nanobelts, to form an NVO/AC composite. The porous AC framework provides a conductive matrix with high surface area and large pore volume for efficient sulfur encapsulation and physical confinement of polysulfides. Meanwhile, the incorporated NVO introduces abundant polar V–O sites and mixed-valence redox-active centers, enabling strong chemical adsorption of polysulfides and catalyzing their bidirectional redox conversion. Owing to this synergistic design, the NVO/AC cathode delivers a high discharge capacity of 1476.9 mA h g^{-1} at 0.1 C. These results demonstrate that combining layered ammonium vanadium oxide electrocatalysts with biomass-derived porous carbon hosts offers a practical and efficient strategy for improving the electrochemical performance of Li–S batteries.

Keywords: Lithium–sulfur batteries, Vanadium-based catalyst, Biomass, Activated carbon, Polysulfide conversion

View Article Online
DOI: 10.1039/D6QI00145A

1. Introduction

Lithium–sulfur (Li–S) batteries have emerged as a promising alternative to conventional lithium-ion batteries due to their exceptional theoretical specific capacity of 1675 mA h g^{-1} and high energy density of approximately 2600 W h kg^{-1}.[1] Compared to nickel-cobalt-manganese (NCM) cathode materials, sulfur offers several advantages, including its natural abundance, environmental benignity, and low cost.[2] However, despite these intrinsic benefits, the practical implementation of Li–S batteries is still hindered by several fundamental challenges. In particular, the inherently low electrical conductivity of sulfur significantly limits the charge-transfer efficiency. Moreover, during cycling, sulfur undergoes complex multistep electrochemical reactions that generate intermediate lithium polysulfides (LiPSs) species.[3, 4] These polysulfides are highly soluble in organic electrolytes and readily migrate between the cathode and anode, giving rise to the so-called shuttle effect. This undesirable phenomenon leads to continuous loss of active materials, low coulombic efficiency, severe capacity fading, and poor cycling stability, thereby posing significant obstacles to the commercialization of Li–S batteries.

To address these issues, various carbon-based materials have been widely explored as sulfur host matrices, including carbon nanofibers (CNFs),[5, 6] carbon nanotubes (CNTs),[7, 8] reduced graphene oxide (rGO),[9, 10] and porous carbon structures.[11, 12] These carbonaceous frameworks provide continuous electron-conduction pathways that partially alleviate the insulating nature of sulfur, while their porous architectures enable physical confinement of sulfur species and accommodate the large volumetric expansion associated with sulfur conversion during cycling. Among them, biomass-derived activated carbon (AC) has attracted particular interest owing to its low cost, abundant and renewable precursors, well-developed porous structures, and sustainability from a circular-economy perspective. The large specific surface area and pore volume of AC allow for high sulfur loading and improved electrolyte infiltration, thereby enhancing sulfur utilization. In addition, the carbon framework contributes to maintaining structural integrity during repeated charge–discharge processes.[13, 14] Nevertheless, despite these promising attributes, AC is not sufficient to fully overcome the challenges associated with Li–S batteries. A major limitation arises from its nonpolar nature, which results in weak interactions with

View Article Online
DOI: 10.1039/D6QI00145A

polar LiPSs. [15] As a result, LiPS retention is inadequate, and the shuttle effect remains a persistent issue.

To overcome the intrinsic limitations of nonpolar carbon hosts, the incorporation of polar electrocatalytic components has been proposed as an effective strategy to chemically immobilize LiPSs and accelerate the redox conversion of LiPSs. In this context, various transition-metal-based catalysts, such as transition metal oxides, [16-18] carbides, [19-21] nitrides, [22, 23] and sulfides, [24, 25] have been integrated into sulfur cathodes to regulate sulfur redox chemistry. These polar materials can provide strong chemical interactions with LiPSs and reduce the activation energy for sulfur reduction and Li_2S oxidation, thereby suppressing the shuttle effect and improving reaction kinetics.

Among various candidates, vanadium (V)-based materials have attracted considerable interest owing to their unique electronic structures and versatile oxidation states. Both theoretical calculations and experimental studies have demonstrated that V-based catalysts exhibit strong chemical adsorption toward LiPS intermediates and significantly reduced energy barriers for bidirectional sulfur redox reactions. [26] In particular, vanadium oxides, such as V_2O_5 and VO_2 containing polar V–O bonds, have been reported to act as effective polysulfide anchors and catalytic centers when employed as interlayers or hybrid sulfur hosts, thereby enhancing reaction kinetics, rate capability, and cycling stability. [27-29] Nevertheless, conventional vanadium oxides often suffer from the limited electrical conductivity, which restricts their effectiveness in fully regulating polysulfide conversion in Li–S batteries.

Ammonium vanadium oxide ($(NH_4)V_4O_{10}$, NVO) represents a distinctive layered vanadium oxide composed of corner- and edge-sharing VO_x polyhedra separated by NH_4^+ pillars. [30-33] This unique structure exposes abundant polar V–O sites and accommodates mixed-valence vanadium species (V^{4+}/V^{5+}), which synergistically contribute to both polysulfide anchoring and catalytic conversion. Specifically, the polar V–O bonds provide strong electrostatic interactions with the Li^+ moieties of LiPSs, enabling robust chemisorption. Meanwhile, the V^{4+}/V^{5+} redox couple operates as an electron-transfer relay: V^{5+} centers accept electrons from soluble LiPSs to facilitate their reduction toward shorter-chain species and Li_2S during discharge, while V^{4+} centers donate electrons to promote Li_2S oxidation during charging. This reversible V^{4+}/V^{5+} interconversion establishes a dynamic redox balance

View Article Online
DOI: 10.1039/D6QI00145A

that accelerates the bidirectional sulfur redox. [34] Moreover, the layered architecture of NVO can facilitate interfacial electron transport and provides multiple redox-active centers associated with its mixed-valence nature. [35-41] These characteristics suggest that NVO could serve as an efficient catalytic platform for regulating polysulfide conversion in Li–S batteries. Despite these promising attributes, the application of NVO as a functional component in Li–S batteries has remained largely unexplored.

Herein, we report the rational design and synthesis of a biomass-derived activated carbon (AC)-supported ammonium vanadium oxide (NVO) composite (NVO/AC) as a multifunctional sulfur host for high-performance Li–S batteries. Waste coffee grounds were upcycled into highly porous AC, providing a conductive framework with a large pore volume for sulfur encapsulation and physical confinement of polysulfides. Polar NVO nanobelts were subsequently grown in situ on the AC surface, constructing a heterogeneous hybrid architecture that integrates the conductivity and structural advantages of carbon with the strong chemical adsorption and electrocatalytic activity of NVO. In this hybrid architecture, the porous carbon framework ensures efficient electron transport and sulfur accommodation, while the uniformly distributed NVO offers abundant polar V–O sites and redox-active centers to chemically anchor LiPSs and catalyze their bidirectional conversion. Density functional theory (DFT) calculations reveal that the NVO surface exhibits significantly stronger chemisorption toward LiPSs than nonpolar or oxygen-functionalized carbon, which is favorable for suppressing polysulfide shuttling. Consistent with these theoretical insights, electrochemical analyses demonstrate that the NVO/AC composite effectively accelerates polysulfide conversion kinetics and improves interfacial charge-transfer processes. Consequently, the synergistic integration of AC and NVO leads to enhanced sulfur utilization, suppressed shuttle effect, and improved rate capability and cycling stability in Li–S batteries.

View Article Online
DOI: 10.1039/D6QI00145A

2. Experimental

2.1. Synthesis of AC

In this work, the AC was synthesized by using waste coffee grounds (Starbucks) and potassium hydroxide (KOH, 95.0%, Samchun) as starting materials. Coffee grounds were dispersed in deionized water by sonication, followed by centrifugation. The resulting solid was then washed with deionized water and ethanol, and dried at 80 °C in a vacuum oven overnight. Subsequently, the dried product was calcined for 2 h in air at 350 °C, with a heating rate of 5 °C min^{-1}. The heat-treated powder and KOH were then ground together at a weight ratio of 1:3, and the resulting mixture was calcined at 800 °C (ramp rate = 5 °C min^{-1}) for 1 h under an argon atmosphere. After that, the calcined powder was dispersed in 200 mL of deionized water, and hydrochloric acid (HCl, 37%, Duksan) was added to adjust the pH to 7. The solution was then centrifuged and washed with deionized water and ethanol. Finally, the obtained product was dried at 80 °C and vacuum–dried overnight.

2.2. Synthesis of NVO/AC

The NVO/AC was synthesized via a hydrothermal method. First, 90 mg of ammonium metavanadate (NH_4VO_3, 99.0%, Samchun) was dissolved in 50 mL of a solution containing ethanol and deionized water (1:9 by volume), and then AC was added. After that, HCl was added to adjust the pH to 2, and the mixture was stirred for 60 min. The resulting solution was transferred to a 100 mL Teflon-lined autoclave and heated at 140 °C for 2, 6, 10, 14, or 20 h to investigate the effect of reaction time. After the reaction, the solution was centrifuged and washed with deionized water and ethanol, and the obtained product was dried overnight at 80 °C. Finally, the dried product was calcined at 400 °C (ramp rate = 5 °C min^{-1}) for 1 h under an argon atmosphere

2.3. Synthesis of S/NVO/AC composites

For the composite synthesis, sulfur was incorporated into the NVO/AC host to obtain the sulfur-loaded NVO/AC composite (S/NVO/AC) by mixing NVO/AC and sulfur at a weight ratio of 1:3, followed by vacuum sealing and heat treatment at 155 °C for 12 h. For comparison, a sulfur-loaded

View Article Online
DOI: 10.1039/D6QI00145A

activated carbon composite (S/AC) was prepared using the same procedure.

2.4. Material characterization

The crystal structures of the as-synthesized samples were analyzed by X–ray diffractometry (XRD; SmartLab, Rigaku), while the specific surface areas and pore size distributions were determined by Brunauer–Emmett–Teller analysis (BET; ASAP 2460, Micromeritics). The chemical states of the elements were investigated via X–ray photoelectron spectroscopy (XPS; MultiLab 2000, Thermo Fisher Scientific), and the Raman spectra were recorded using a laser Raman spectrophotometer (NRS–5100, JASCO). The sample morphologies were examined by transmission electron microscopy (TEM; EM–2010, JEOL) and field emission scanning electron microscopy (FE–SEM; JSM–7900F, JEOL), while the elemental compositions were determined via energy dispersive spectrometry (EDS).

2.5. Electrochemical characterization

For electrochemical characterization, a slurry was prepared consisting of 70 wt% active materials, 20 wt% conductive additive (carbon black; Thermo Fisher Scientific), and 10 wt% binder (polyvinylidene fluoride (PVDF; MTI Korea)) in *N*-methyl pyrrolidone (NMP; Sigma Aldrich). This slurry was then coated onto carbon-coated aluminum foil and dried at 70 ºC overnight. The loading mass of the active material was 1.0–1.5 mg cm^{-2}. A coin cell was assembled in a standard CR2032 configuration inside an argon-filled glovebox with a moisture content below 0.1 ppm. The electrolyte was prepared by dissolving 1 M lithium bis(trifluoromethanesulfonyl)imide (LiTFSI; Sigma Aldrich) in a 1:1 (v/v) mixture of 1,2-dimethoxyethane (DME; Sigma Aldrich) and 1,3-dioxolane (DOL; Sigma Aldrich), with the addition of 1 wt% lithium nitrate ($LiNO_3$). Celgard 2400 was used as the separator. Galvanostatic charge–discharge (GCD) measurements were performed using a battery tester (WBCS 3000, WonATech, South Korea) within the voltage range of 1.7–2.8 V (vs. Li/Li^+). Meanwhile, cyclic voltammetry (CV) measurements were obtained at various scan rates by using an electrochemical workstation (CHI440C, CH Instruments) within the same voltage range as the GCD tests. Galvanostatic intermittent titration technique (GITT) measurements were collected at a current density of 0.1 C for 10 min with a rest interval of 10 min. The electrochemical impedance spectroscopy (EIS) data were

View Article Online
DOI: 10.1039/D6QI00145A

acquired using a ZIVE SP1 (WonATech, South Korea) over the frequency range of 10 mHz to 100 kHz, and were fitted using ZMAN software.

2.6. Preparation and adsorption test of the Li_2S_6 electrolyte

To prepare the 5 mM Li_2S_6 electrolyte, a 1:5 molar ratio of lithium sulfide (Li_2S; Thermo Fisher Scientific) and sulfur (S; Samshun) was dissolved in a 1:1 (v/v) mixture of DME and DOL, followed by stirring. After that, 4 mL of Li_2S_6 solution was added to each AC and NVO/AC sample, and the adsorption effect was evaluated by monitoring the color change over time.

2.7. Assembly and measurement of the symmetric cells

Symmetric cells containing the AC or NVO/AC samples were assembled as coin cells by placing two identical sulfur-free electrodes between a Celgard 2400 separator, followed by addition of the Li_2S_6 electrolyte. After that, CV measurements were performed at 0.1 mV using an electrochemical workstation (CHI440C, CH Instruments) in the voltage range of –1.5 to 1.5 V.

2.8. Preparation and precipitation test of the Li_2S_8 electrolyte

For this procedure, a 0.5 M Li_2S_8 catholyte was prepared by dissolving 1:7 (mol/mol) Li_2S and S in tetraethylene glycol dimethyl ether (TEGDME; Sigma Aldrich) and stirring at 60 °C for 12 h. The Li_2S deposition test was conducted using a battery tester (WBCS 3000, WonATech). The cell was assembled using sulfur-free electrodes along with the as-prepared Li_2S_8 electrolyte. The cell was discharged to 2.06 V at a constant current of 0.112 mA, followed by a potentiostatic hold at 2.05 V, during which Li_2S deposition was monitored.

2.9. Compuational methods

Density functional theory (DFT) calculations were performed using the Vienna Ab initio Simulation Package (VASP). [42] The electron exchange-correlation interactions were described by the generalized gradient approximation (GGA) with the Perdew–Burke–Ernzerhof (PBE) functional, [43] and the projector augmented wave (PAW) method was employed to treat the core–valence electron interactions. [44] A plane-wave cutoff energy of 400 eV was used for all calculations. The Monkhorst–Pack k-point

View Article Online
DOI: 10.1039/D6QI00145A

meshes of 3 × 3 × 1 and 3 × 5 × 1 were used for the graphene-based models and the NVO (001) slab, respectively. A vacuum layer of 15 Å was introduced in the z-direction to avoid spurious interactions between periodic images, and dipole corrections were applied along the surface normal direction.

View Article Online
DOI: 10.1039/D6QI00145A

3. Results and discussion

As detailed in the experimental section and shown schematically in Fig. 1, the AC was prepared from spent coffee grounds via a two-step thermal treatment and KOH activation. Briefly, the washed and dried coffee waste was first carbonized and then chemically activated with KOH at an elevated temperature to yield a highly porous AC host. The NVO/AC composite was then prepared by hydrothermal growth of NVO on the AC surface, followed by post-annealing at 400 °C, yielding crystalline NVO nanobelts uniformly anchored on the AC framework.

The crystal structures of the as-synthesized AC and NVO/AC samples are revealed by the XRD results in Fig. 2a. Notably, no distinct peaks are observed in the AC spectrum, whereas the NVO/AC sample exhibits characteristic diffraction peaks corresponding to the (001), (002), ($\bar{2}$02), (110), (003), (400), ($\bar{3}$11), ($\bar{2}$05), (020), and ($\bar{7}$12) crystalline planes of $(NH_4)V_4O_{10}$ (JCPDS No. 31-0075). This crystal structure belongs to the monoclinic system with the C2/m space group. [45, 46]

The structural characteristics of the as-synthesized materials are revealed by the corresponding Raman spectra in Fig. 2b and c. In the range of 1200–1800 cm^{-1} (Fig. 2b), two distinct peaks are observed, including the D band (originating from disordered carbon) at approximately 1350 cm^{-1} and the G band (associated with graphitic ordered carbon) near 1600 cm^{-1}. [47, 48] The comparable I_D/I_G ratios of AC and NVO/AC suggest that the hydrothermal synthesis process does not induce significant structural changes in the carbon matrix. In the range of 100–1200 cm^{-1} (Fig. 2c), however, no distinct peaks are observed for the AC sample, while multiple peaks are present in the NVO/AC sample, suggesting that these peaks originate from the NVO component. [49-52] The low-frequency Raman region typically reflects external modes of the lattice, including the bending and wagging modes. The peak at 150 cm^{-1} is attributed to the external lattice vibration mode of the V–O–V linkages, while those at 201 and 994 cm^{-1} correspond to the respective wagging and stretching vibrations of the terminal V=O bonds. Additional peaks are observed at 290 and 415 cm^{-1} due to the bending vibration of the V=O double bond in the O_3–V=O configuration and the bending vibration of the V–O_3–V bond. Meanwhile, the peak at 699 cm^{-1} corresponds to the symmetric stretching vibration of the V–O–V linkage.

View Article Online
DOI: 10.1039/D6QI00145A

The pore structures of the AC and the NVO/AC composite are characterized by the N_2 adsorption–desorption isotherms in Fig. 2d, while the corresponding surface area and pore volume data are summarized in Table 1. The AC exhibits a typical Type I isotherm, which is indicative of a microporous structure, with a high specific surface area of 2589.8 $m^2\ g^{-1}$ and a total pore volume of 1.1267 $cm^3\ g^{-1}$. By contrast, the NVO/AC composite exhibits a slightly lower surface area of 2503 $m^2\ g^{-1}$ but a larger pore volume of 1.6951 $cm^3\ g^{-1}$. Notably, the NVO/AC composite exhibits a hybrid Type I/IV isotherm, characterized by a sharp uptake at low relative pressure ($P/P_0 < 0.1$), suggesting the preservation of microporosity from the AC host, while the distinct hysteresis loop in the intermediate P/P_0 range of 0.4–0.9, demonstrates the introduction of mesoporosity. These pore characteristics are further confirmed by the BJH pore size distribution analysis in Fig. 2e. The AC exhibits negligible mesoporosity in the 2–50 nm range due to its microporous nature, whereas the NVO/AC composite shows a clear pore peak at around 4 nm. Such a hierarchical pore structure is expected to provide a more favorable physical confinement environment for sulfur species. The sulfur loadings of the S/NVO/AC and S/AC composites were evaluated by TGA, as shown in Fig. 2f. Consistent with their large pore volumes, the AC and NVO/AC samples exhibit high sulfur loadings of approximately 75% and 73%, respectively.

The surface chemical states of the AC and NVO/AC samples are analyzed by the XPS results in Fig. 2g–i. The high-resolution O 1s spectra (Fig. 2g) show the appearance of an additional peak at 529.6 eV for the NVO/AC composite, which is absent from the AC. This peak is characteristic of the lattice oxygen associated with V–O bonds and is therefore indicative of the presence of NVO in the composite. Similarly, the V 2p spectra in Fig. 2h show no discernible signals for the AC, whereas the NVO/AC exhibits characteristic V $2p_{3/2}$ and V $2p_{1/2}$ doublets. The peaks at 515.7/523.4 eV and 517.1/524.7 eV are assigned to V^{4+} and V^{5+}, respectively (V $2p_{3/2}$/V $2p_{1/2}$), suggesting the coexistence of mixed-valence vanadium species in the composite. The coexisting V^{4+}/V^{5+} species are expected to serve as efficient electron-transfer mediators that facilitate the catalytic conversion of LiPSs. As reported for vanadium-based electrocatalysts, high-valence V^{4+}/V^{5+} centers function as strong electron acceptors capable of distorting LiPS intermediates and facilitating the cleavage of S–S and Li–S bonds, while the reversible

View Article Online
DOI: 10.1039/D6QI00145A

interconversion among vanadium valence states establishes a dynamic redox balance that accelerates stepwise sulfur transformations. [34] Likewise, the N 1s spectrum in Fig. 2i displays no detectable N-related signals for the pure AC, while the NVO/AC presents a distinct peak at 400.3 eV, which can be attributed to nitrogen species originating from NH_4^+ in the NVO structure.

The morphologies of the AC and NVO/AC samples are characterized by SEM, as shown in Fig. 3a–d. As shown in Fig. 3a, the AC exhibits a three-dimensional porous architecture with various pore sizes, which facilitates electrolyte penetration and provides a favorable environment for sulfur immobilization. Meanwhile, the images in Fig. 3b and c clearly reveal the uniform growth of NVO nanobelts with an average width of 68.4 $\pm$ 25.3 nm on the carbon surface in the NVO/AC composite. The evolution of this NVO morphology depending on the hydrothermal reaction time at a fixed temperature of 140 ℃ is further revealed by the SEM images in Fig. S1 of the Supporting Information. At a reaction time of 2 h, flower-like NVO structures are dispersed on the AC surface. As the reaction time is increased, the NVO is seen to grow gradually, and the NVO morphology transitions into well-defined nanobelt structures that form a dense and interconnected network.

The distributions of C, N, O, and V in the NVO/AC composite are revealed by the SEM image and corresponding elemental mapping results in Fig. 3d. All elements are uniformly distributed throughout the carbon matrix, suggesting the homogeneous growth of NVO on the AC framework. Further insights into the crystal structure of the NVO/AC are provided by the TEM images in Fig. 3f and g. The NVO/AC composite displays a thin nanobelt morphology with distinct lattice fringes, in which the interplanar distances of 0.48 and 0.349 nm, corresponding to the (002) and (110) planes, respectively. Moreover, the corresponding SAED pattern in Fig. 3h shows well-defined diffraction spots that are indexed to the ($\bar{2}$02), ($\bar{2}$05), and (020) planes, which is in good agreement with the above-mentioned XRD results, confirming the crystalline nature of NVO in the composite. The side-view TEM image of the NVO nanobelts (Fig. S2) reveals lattice fringes corresponding to the (002) plane, further confirming the preferential stacking along the [001] direction and the dominant exposure of the (001) basal plane. This observation is consistent with previous reports on NVO nanobelts, in which the extremely high

View Article Online
DOI: 10.1039/D6QI00145A

intensity of the (001) reflection has been attributed to the preferential exposure of the (001) surface facets. [53]

As discussed above, the polar V–O sites exposed on the NVO surface are expected to provide stronger anchoring sites for LiPSs compared to the nonpolar carbon framework. To theoretically validate this hypothesis, DFT calculations were performed to compare the binding energies of representative polysulfide species (Li_2S_4 and Li_2S_6) on various carbon-based surfaces and the NVO (001) surface (Fig. S3). As shown in Fig. 4a, pristine graphene and defect-graphene exhibit negligible binding energies toward both Li_2S_4 and Li_2S_6, which is consistent with the well-known nonpolar nature of sp^2 carbon that results in weak van der Waals interactions with polar LiPS molecules. The introduction of oxygen functional groups (*O and *OH) onto the carbon surfaces moderately enhances the binding strength, yielding binding energies in the range of −0.4 to −0.7 eV. These values correspond to weak physisorption or incipient chemisorption, which is insufficient to effectively anchor LiPS molecules. In stark contrast, the NVO (001) surface exhibits substantially stronger binding energies of −1.78 eV for Li_2S_4 and −1.33 eV for Li_2S_6, indicating robust chemisorption. A similar trend was also obtained for the NVO (100) surface in additional calculations (Fig. S4), with binding energies of −2.31 eV for Li_2S_4 and −1.99 eV for Li_2S_6, suggesting that strong LiPS adsorption is not limited to the basal-plane model and may also persist at edge/side-facet-like exposed surfaces. This remarkable enhancement can be attributed to the unique electronic structure of NVO. Due to the presence of NH_4^+ pillars intercalated between the V_4O_{10} layers, the exposed (001) surface possesses an anionic character with an excess electron density of approximately 2.09 e nm^{-2}. This negatively charged surface provides abundant electrostatic interaction sites for the Li^+ moieties of LiPSs. The optimized adsorption configurations on graphene, defect-graphene, and NVO (001) surfaces are presented in Fig. 4b and c for Li_2S_4 and Li_2S_6, respectively. On the oxygen-functionalized carbon surfaces, LiPSs interact predominantly through the *OH group via Li–O coordination, whereas on the NVO surface, multiple Li–O interactions are established, thereby leading to a more stable adsorption geometry. The differential charge density analysis further elucidates the distinct adsorption mechanisms (Fig. S5). For Li_2S_4 adsorbed on the graphene–OH surface, charge redistribution is localized primarily at the Li–O interface

View Article Online
DOI: 10.1039/D6QI00145A

with limited polarization of the adsorbate. In contrast, the NVO (001) surface induces pronounced charge polarization throughout both the adsorbate and the surface region. This enhanced interfacial charge poliarization facilitates stronger chemical bonding and is expected to promote more efficient electron transport during the electrochemical conversion of LiPSs.

These theoretical predictions are experimentally supported by the LiPS adsorption test results shown in Fig. 4d. No obvious color change is observed in the AC-containing solution, whereas the color of the NVO/AC-containing solution gradually faded over time. After 12 h, the NVO/AC solution has become almost colorless, suggesting a strong adsorption of LiPSs. The catalytic effects of the AC and NVO/AC electrodes on LiPS conversion were further investigated using symmetric cells, as elucidated by the CV profiles obtained in the voltage range of –1.5 to 1.5 V at a scan rate of 5 mV s^{-1} in Fig. 4e. Compared with the AC electrode, the NVO/AC electrode exhibits a higher current, indicating enhanced electrochemical activity toward LiPS conversion. Moreover, the enhanced redox activity and higher LiPS conversion capability of the NVO/AC are indicated by redox peaks at ±0.098 V and ±0.311 V, whereas the AC electrode only exhibits redox peaks at ±0.098 V. The corresponding Tafel curves are presented in Fig. 4f. The exchange current density (i_0) was estimated from the Tafel plots according to the Tafel equation, given as eqn (1): [54]

$$\eta = a + b \log i \qquad (1)$$

where η is the overpotential, a is a constant, b is the Tafel slope, and i is the current density (mA cm^{-2}). Accordingly, the NVO/AC exhibits a higher exchange current density of 0.063 mA cm^{-2} compared to 0.038 mA cm^{-2} for the AC, suggesting faster charge-transfer kinetics for the NVO/AC in Li–S batteries.

The Li_2S precipitation kinetics are investigated by the potentiostatic discharge curves of the AC and NVO/AC electrodes in Li_2S_8 -containing solvent in Fig. 4g and h, respectively. From these results, the Li_2S precipitation capacities were estimated according to Faraday's law. The NVO/AC electrode delivers a capacity of 63.56 mA h g^{-1}, which is significantly higher than that of the AC electrode (14.83 mA h g^{-1}), indicating enhanced catalytic activity of NVO in facilitating the redox conversion of LiPSs.

View Article Online
DOI: 10.1039/D6QI00145A

In Fig. 4i and j, the kinetic behaviors of the AC and NVO/AC electrodes are characterized according to four classical models, including the Bewick, Fleischman, and Thirsk (BFT) models and the Scharifker–Hills (SH) models. [55-57] The relevant equations are provided as eqns. S1–S4. In the BFT models, 2DI and 2DP indicate two-dimensional (2D) instantaneous and progressive nucleation, respectively. In the SH models, 3DI and 3DP indicate three-dimensional (3D) instantaneous and progressive nucleation, respectively. The results indicate that the precipitation of Li_2S on pure AC is consistent with the 2DI mechanism, whereas the behavior of the NVO/AC electrode more closely approximates the 3DP model, suggesting a more three-dimensional and sustained Li_2S growth in the presence of NVO. According to previous reports, 2DI growth tends to form a laterally extended, film-like insulating Li_2S layer that can induce early surface passivation, whereas 3DP growth promotes more spatially distributed Li_2S precipitation, which helps preserve charge-transfer pathways during the precipitation process. 43–45 Therefore, this shift toward 3DP-like Li_2S growth in the NVO/AC electrode is expected to be beneficial for mitigating premature electrode passivation and preserving charge-transfer pathways during precipitation. In the NVO/AC architecture specifically, the uniformly distributed NVO nanobelts on the porous AC surface provide abundant and spatially dispersed nucleation sites, which promotes volumetric Li_2S deposition rather than lateral film growth. This structural advantage, combined with the catalytic activity of NVO, contributes to a higher Li_2S yield and improved reversibility of LiPS redox reactions, ultimately enhancing sulfur utilization and cycling stability. Consequently, a higher Li_2S yield and improved reversibility of LiPS redox reactions are expected, which contributes to enhanced sulfur utilization and cycling stability.

The redox behaviors of the Li–S half-cells containing the as-synthesized cathodes during the charge–discharge process are revealed by the CV measurements obtained in the voltage range of 1.7–2.8 V at various scan rates of 0.1–0.5 mV s^{-1} in Fig. 5a and b. As the scan rate is increased, the NVO/AC exhibits a higher current density than the AC, indicating that the catalytic effect of NVO facilitates faster redox reaction kinetics. Furthermore, as the scan rate increases, the anodic and cathodic peak positions of AC shift more noticeably than those of NVO/AC, suggesting that the internal resistance of the pure AC is more strongly affected by the scan rate. Meanwhile, the precise onset potentials of the anodic and

View Article Online
DOI: 10.1039/D6QI00145A

cathodic redox reactions are determined from the plots of differential current density against voltage in Fig. 5c and d. The anodic reaction of NVO/AC is initiated at 2.187 V, whereas that of the AC cathode begins at 2.201 V, suggesting that the NVO effectively lowers the energy barrier for LiPS conversion during charging. Similarly, during discharge, the cathodic reactions initiate at higher potentials of 2.442 and 2.099 V for NVO/AC, compared to 2.430 and 2.098 V for AC, further supporting the role of the catalyst in facilitating LiPS conversion by reducing the energy barrier. [58] This catalytic effect is further corroborated by the Tafel plots in Fig. 5e and f. Thus, in the cathodic region, the AC and NVO/AC exhibit Tafel slopes of 59.72 and 49.29 mV dec^{-1}, respectively, indicating faster reduction kinetics in the presence of NVO. Similarly, in the anodic region, the Tafel slopes are 134.7 and 120.3 mV dec^{-1}, respectively, which suggests different oxidation reaction dynamics that are possibly influenced by the catalytic effect. [59] In addition, the CV curves show a linear relationship between the peak current and the square root of the scan rate, which reflects Li-ion diffusion behavior, in accordance with the Randles–Sevcik equation, given here as eqn (2):

$$I_p = (2.69 \times 10^5)\, n^{1.5} A\, D^{0.5} C v^{0.5} \quad (2)$$

where I_p is the peak current (A), n is the number of electrons involved in the redox reaction, A is the electrode area (cm^2), D is the diffusion coefficient of Li^+ ions ($cm^2\ s^{-1}$), C is the concentration of the electroactive species in the electrolyte (mol cm^{-3}), and v is the scan rate (V s^{-1}). Based on the CV curves of the AC and NVO/AC electrodes, the linear relationships between the peak current and the square root of the scan rate are plotted for two anodic and two cathodic peak currents in Fig. S6. The slopes of these plots, which reflect the Li-ion diffusion coefficients, are consistently larger for NVO/AC than for AC, indicating faster Li-ion diffusion across all redox processes. [60]

The internal resistances of the AC and NVO/AC electrodes under dynamic conditions are elucidated by the GITT results in Fig. S7 and Fig. 5g and h. The voltage measured at the end of each 10-min rest period is regarded as the open circuit voltage (OCV), whereas the sudden voltage response recorded immediately after current application is defined as the closed circuit voltage (CCV). From these measurements, the AC electrode exhibits IR drops of 16 mV during discharge (Fig. S7a) and 9 mV

View Article Online
DOI: 10.1039/D6QI00145A

during charge (Fig. S7b), whereas the NVO/AC electrode exhibits lower values of 8.0 and 6.7 mV, respectively (Fig. S7c and d). These results indicate that the instantaneous response upon current application is reduced in the NVO/AC electrode, suggesting a decrease in IR overpotential due to the catalytic effect of NVO. The internal resistance during the charge and discharge processes can be calculated using eqn (3): [61, 62]

$$\Delta R = \frac{|\Delta V_{OCV-CCV}|}{I_{applied}} \quad (3)$$

The results in Fig. 5i indicate that, during the charging process, the NVO/AC exhibits a lower internal resistance than AC. Moreover, after prolonged cycling, the NVO/AC also exhibits a reduced internal resistance during the discharging process. These results demonstrate that the incorporation of NVO contributes to reduced internal resistance, which is beneficial for improving the electrochemical performance of Li–S batteries.

The resistance of each sample is further evaluated from the EIS Nyquist plots in Fig. S8. The NVO/AC exhibits a charge transfer resistance of 16.3 Ω, which is significantly lower than that of the AC (30.9 Ω), indicating more efficient charge-transfer processes in the presence of NVO. This trend is consistent with the internal resistance values calculated from the GITT results.

The electrochemical performance of the NVO/AC and AC electrodes at various current densities are evaluated by the GCD profiles obtained during five cycles at C-rates of 0.1, 0.2, 0.5, 1, 2, 3, and 5 C in Fig. 6a–c. At 0.1 C, the AC exhibits an initial discharge capacity of only 1190.7 mA h g^{-1}, whereas the NVO/AC cathode delivers a significantly higher initial capacity of 1476.96 mA h g^{-1}. Moreover, the NVO/AC cathode maintains excellent discharge capacities of 974.7, 827.0, 711.1, 569.1, 476.9, and 375.0 mA h g^{-1} at the C-rates of 0.2, 0.5, 1, 2, 3, and 5 C, respectively, and outperforms the AC cathode at all tested rates. To confirm that the performance enhancement of NVO/AC originates from the catalytic function of NVO rather than its intrinsic lithium storage capacity, a sulfur-free NVO/AC electrode was evaluated within the same voltage window of 1.7–2.8 V (Fig. S9). The sulfur-free electrode exhibited negligible capacity across all tested C-rates, confirming that the capacity

View Article Online
DOI: 10.1039/D6QI00145A

contribution of NVO itself is minimal within this operating window. This performance enhancement can be attributed to the catalytic effect of NVO, which lowers the energy barrier for LiPS conversion and accelerates the redox kinetics. These effects suppress polarization, as evidenced by the reduced voltage gap between the charge and discharge plateaus in the GCD curves. For example, at 0.1 C (Fig. 6d), the NVO/AC cathode exhibits a smaller voltage gap of 0.144 V compared to 0.156 V for the AC cathode, indicating reduced polarization and internal resistance. Moreover, the utility of the reduction from Li_2S_n to Li_2S is demonstrated in Fig. S10, which compares the higher and lower specific capacity (Q_H and Q_L) values derived from the initial discharge voltage profiles at 0.1 C (i.e., Fig. 6d). The AC exhibits Q_H and Q_L values of 396 and 794 mA h g^{-1}, respectively, giving a Q_L/Q_H ratio of approximately 2.0. By contrast, the NVO/AC exhibits Q_H and Q_L values of 450 and 1126 mA h g^{-1}, respectively, with a Q_L/Q_H ratio of 2.28. These results indicate that the catalytic effect of NVO enhances the utility of the reduction reaction of LiPS to Li_2S. Additionally, the corresponding differential capacity (dQ/dV) versus potential (V) plots for the AC and NVO/AC during the initial charge-discharge process are presented in Fig. S11. Both samples exhibit features consistent with the CV results, indicating more uniform redox reactions in the NVO/AC electrode during cycling.

The long-term stability of the AC and NVO/AC cathodes in the Li–S system over 300 cycles at a current density of 0.5 C is demonstrated in Fig. 6e. The NVO/AC cathode demonstrates excellent cycling stability, retaining a capacity of 512.99 mA h g^{-1} (59.4% of its initial value) after the 300 cycles, along with an average capacity fade rate of 0.173% per cycle. By contrast, the AC cathode maintains a capacity of 281.67 mA h g^{-1} (51.5% of its initial value) and shows a higher average capacity loss of 0.221% per cycle. In addition, the coulombic efficiency was maintained at around 98% during the 300 cycles, demonstrating good electrochemical reversibility and stable long-term operation. The voltage profiles of the 10^{th} and 100^{th} cycles at 0.5 C are compared in Fig. S12. Despite prolonged cycling, the voltage profile of the NVO/AC electrode maintains a nearly identical shape to that observed for the initial cycle, indicating superior cycling stability due to the catalytic effect of NVO. Overall, the incorporation of the NVO catalyst into the sulfur cathode significantly enhances both the specific capacity and cycling stability of the Li–S battery system, demonstrating the great potential of NVO as

View Article Online
DOI: 10.1039/D6QI00145A

an effective performance-boosting catalyst. The NVO/AC cathode demonstrates superior electrochemical performance relative to previously reported vanadium-based sulfur host materials, as summarized in Table S1. To further assess the structural and chemical integrity of the NVO/AC electrode after prolonged cycling, post-mortem SEM, XRD, and XPS analyses were performed on the cathode after 300 cycles at 0.5 C (Fig. S13). The SEM images (Fig. S13a) reveal that the overall electrode morphology is largely preserved, with NVO nanobelts remaining identifiable on the AC surface without severe agglomeration or detachment, indicating good mechanical integrity during prolonged cycling. The XRD pattern (Fig. S13b) confirms that the characteristic diffraction peaks of the NVO phase are retained after 300 cycles with no emergence of new phases, demonstrating structural robustness under long-term battery operation. Furthermore, the V 2p XPS spectra (Fig. S13c) show that the characteristic V $2p_{3/2}$/V $2p_{1/2}$ peaks at 517.5/525.1 eV (V^{4+}) and 516/523.8 eV (V^{5+}) are both preserved after 300 cycles, confirming that the mixed-valence character of NVO is maintained without irreversible loss of either oxidation state. The N 1s spectrum (Fig. S13d) shows that the peak at 399.2 eV, attributable to NH_4^+ in the NVO framework, remains detectable after prolonged cycling, further supporting the chemical stability of the NVO structure. These results collectively demonstrate that the NVO/AC composite retains its structural and chemical integrity during prolonged cycling, supporting the sustainability of its polysulfide anchoring and catalytic conversion functions.

To verify the electrochemical stability of NVO under real battery operating conditions, ex-situ XRD and XPS analyses were conducted on the NVO/AC electrode at seven selected states of charge across a full discharge–charge cycle at 0.1 C. The ex-situ XRD patterns (Fig. 7a) confirm that the characteristic diffraction peaks of the NVO phase are consistently retained at all states with no emergence of new phases, indicating structural robustness of NVO during electrochemical cycling. The ex-situ V 2p XPS spectra (Fig. 7b) show that both V^{4+} and V^{5+} peaks are preserved throughout the full cycle, confirming that the mixed-valence character of NVO is maintained without irreversible chemical transformation. These results collectively demonstrate that NVO retains structural integrity and chemical stability under practical battery operating conditions.

View Article Online
DOI: 10.1039/D6QI00145A

4. Conclusions

A biomass-derived activated carbon (AC) supported ammonium vanadium oxide (NVO) composite was successfully developed as a multifunctional sulfur host for Li–S batteries. The porous AC framework derived from waste coffee grounds provides a conductive matrix with high surface area and large pore volume, enabling effective sulfur encapsulation and physical confinement of polysulfides. Meanwhile, the NVO nanobelts introduce polar V–O sites and mixed-valence redox-active centers, which strengthen chemical interactions with lithium polysulfides and promote their redox conversion. Experimental and theoretical results demonstrate that the synergistic integration of AC and NVO enhances polysulfide adsorption, accelerates sulfur redox kinetics, and reduces charge-transfer resistance. Density functional theory calculations reveal stronger chemisorption of lithium polysulfides on the NVO surface compared with carbon, while electrochemical analyses, including CV, Tafel, GITT, and Li_2S precipitation measurements, confirm improved reaction kinetics, reduced polarization, and facilitated Li-ion transport. Consequently, the NVO/AC composite cathode exhibits enhanced sulfur utilization, improved rate performance, and superior cycling stability relative to the AC counterpart. This study demonstrates that combining layered ammonium vanadium oxide catalysts with sustainable porous carbon hosts is an effective strategy for regulating polysulfide chemistry and improving the electrochemical performance of Li–S batteries.

View Article Online
DOI: 10.1039/D6QI00145A

Author contributions

Kiseok Lee: Conceptualization, Data curation, Validation, Writing – original draft. Eun Ji Lee: Methodology, Investigation. Hyung-Kyu Lim: Formal analysis. Ji Eun Lee: Funding acquisition, Writing – review & editing.

Conflicts of interest

There are no conflicts to declare.

Data availability

The following data supporting this article have been included as part of the Supplementary Information (SI): SEM, surface model used in the DFT calculation, differential charge density plots, CV peak current relationship, GITT, EIS Nyquist plots, comparative Q_H and Q_L values, plots of dQ/dV versus V, voltage profiles at the 10^{th} and 100^{th} cycles (0.5 C).

Acknowledgements

This work was supported by the National Korea (NRF) (No. RS-2025-00564101) and by the National Research Council of Science & Research Foundation of Technology (NST) (No. GTL24000-000), funded by the Korea government (MSIT).

View Article Online
DOI: 10.1039/D6QI00145A

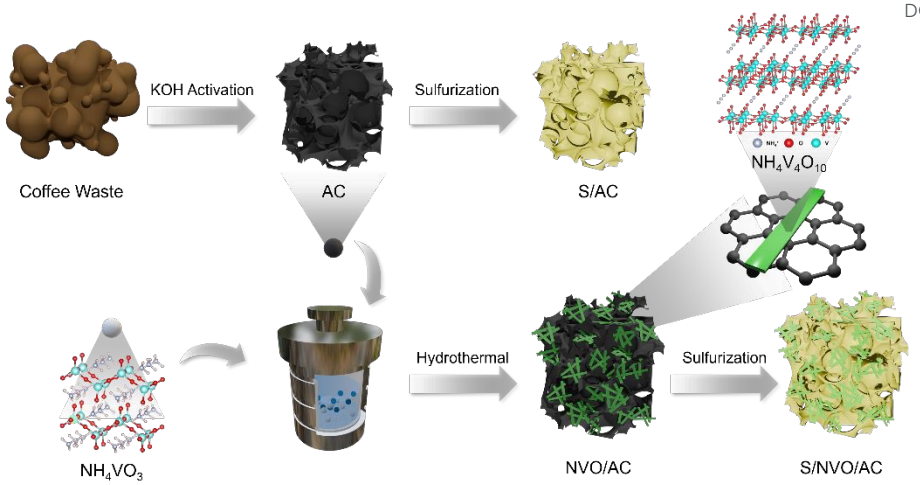

Fig. 1 A schematic diagram showing the synthesis of the AC from waste coffee grounds, and the subsequent preparation of S/AC (top row) and S/NVO/AC (bottom row).

View Article Online
DOI: 10.1039/D6QI00145A

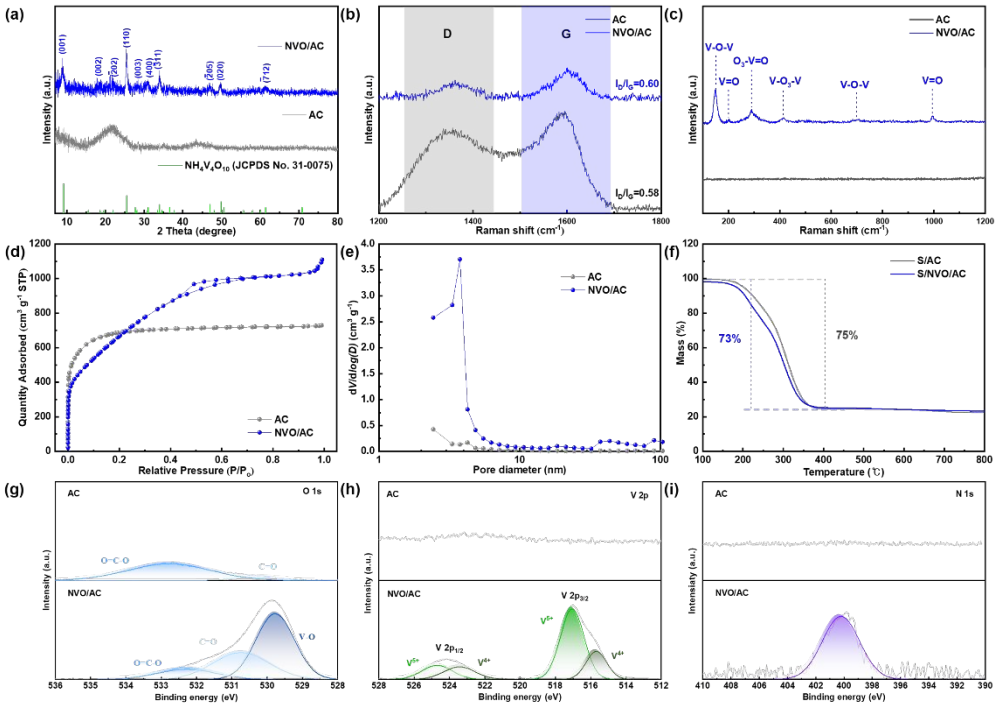

Fig. 2 (a) The XRD patterns of the NVO/AC and AC samples. (b and c) The corresponding Raman spectra in the range of (b) 1200–1800 cm^{-1} and (c) 100–1200 cm^{-1}. (d and e) The N_2–adsorption-desorption curves (d) and pore size distributions (e) of the NVO/AC and AC samples. (f) The thermogravimetric analysis (TGA) curves of the S/NVO/AC and S/AC samples. (g–i) The O 1s (g), V 2p (h), and N 1s (i) XPS spectra of the NVO/AC and AC samples.

Table 1. The specific surface areas, total pore volumes, and average pore diameters of the AC and NVO/AC samples, as calculated from the N_2 sorption measurements via the BET and BJH methods.

Sample	Surface area (m^2 g^{-1})	Pore volume (cm^3 g^{-1})	Mean pore diameter (nm)
AC	2589.8	1.1267	1.7403
NVO/AC	2503	1.6954	2.7095

View Article Online
DOI: 10.1039/D6QI00145A

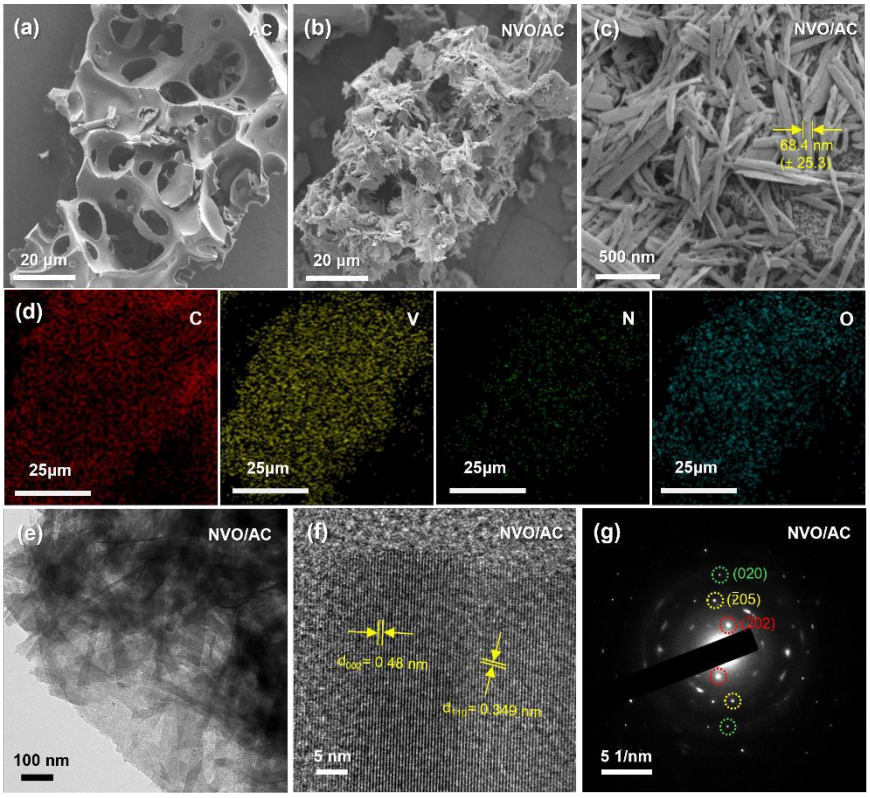

Fig. 3 (a–c) SEM images of (a) the AC and (b and c) the NVO/AC. (d) Elemental maps of the NVO/AC composite. (e–g) The TEM images (e and f) and SAED pattern (g) of the NVO/AC.

View Article Online
DOI: 10.1039/D6QI00145A

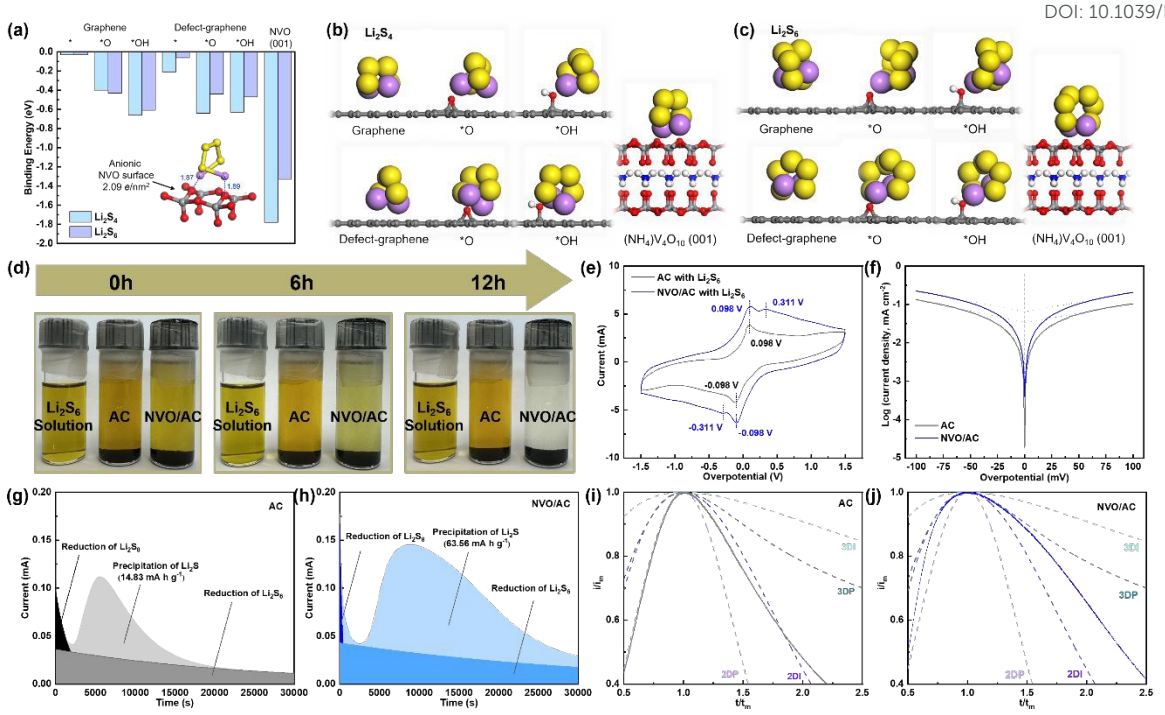

Fig. 4 (a) DFT-calculated binding energies of Li_2S_4 and Li_2S_6 on pristine graphene, defect-graphene, oxygen-functionalized graphene (*O and *OH), and the anionic NVO (001) surface. (b and c) Optimized adsorption configurations of (b) Li_2S_4 and (c) Li_2S_6 on each surface. (d) Photographic images showing the color changes in the AC and NVO/AC powders after 0, 6, and 12 h of exposure to a Li_2S_6 solution. (e) The CV profiles of symmetric cells containing the AC (gray) and NVO/AC (blue) with the Li_2S_6 electrolyte at a scan rate of 5 mV s^{-1}. (f) The corresponding Tafel curves. (g and h) The potentiostatic discharge curves of (g) AC and (h) NVO/AC in a 0.5 M Li_2S_8 solvent at 2.05 V. (i and j) The dimensionless transients of the AC (i) and NVO/AC (j) compared with theoretical 2D and 3D models.

View Article Online
DOI: 10.1039/D6QI00145A

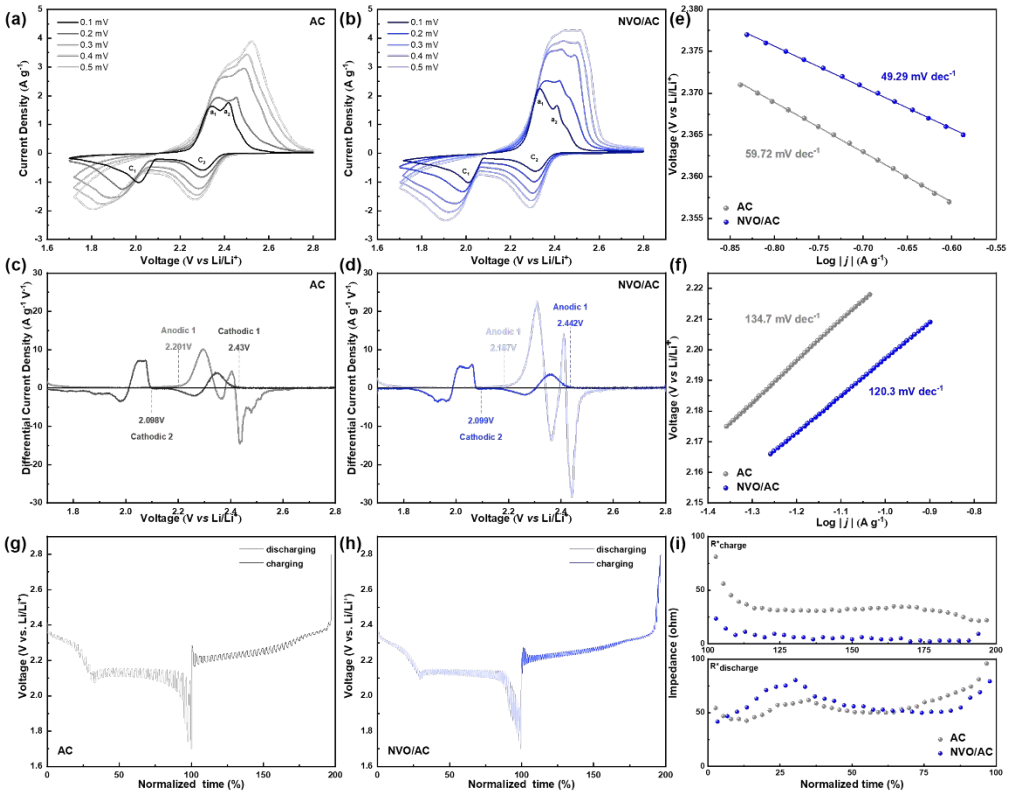

Fig. 5 (a and b) The CV profiles of (a) the AC and (b) the NVO/AC at various scan rates (0.1–0.5 mV^{-1}). (c and d) Differential CV curves of (c) the AC and (d) the NVO/AC at a scan rate of 0.1 mV^{-1}. (e and f) The corresponding Tafel plots in (e) the cathodic region and (f) the anodic region. (g and h) The GITT graphs of (g) the AC and (h) the NVO/AC electrodes. (i) The calculated resistance values of the AC and NVO/AC during the charge (top) and discharge (bottom) processes.

View Article Online
DOI: 10.1039/D6QI00145A

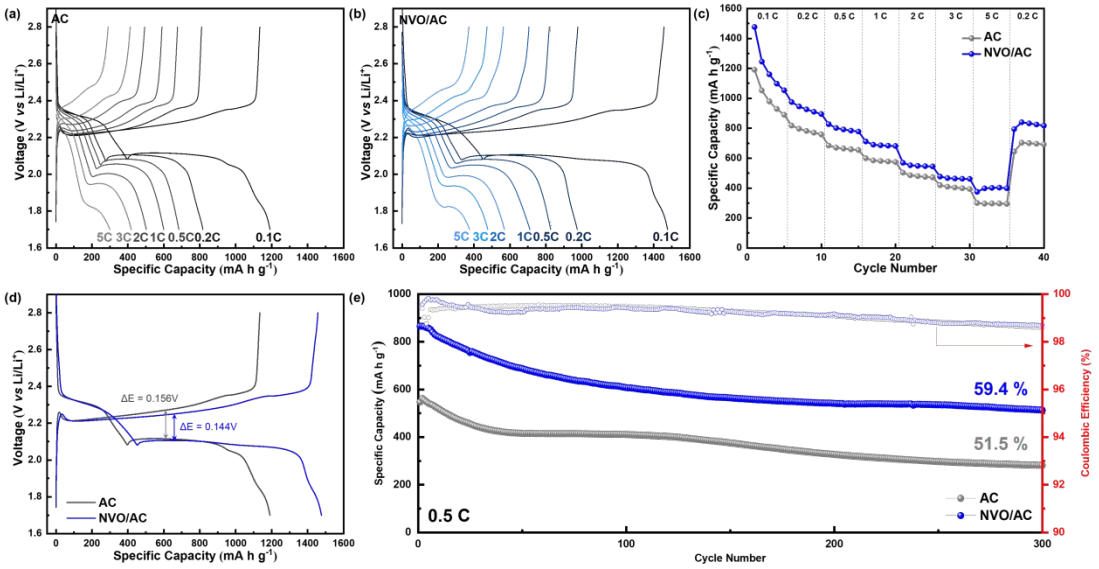

Fig. 6 (a and b) The GCD profiles of (a) the AC electrode and (b) the NVO/AC electrode at various C-rates. (c) The rate performance of the AC electrode (gray) and NVO/AC electrode (blue) at various C-rates. (d) The GCD profiles of the AC and NVO/AC electrodes at 0.1 C. (e) The cycling performance of the AC and NVO/AC electrodes at 0.5 C.

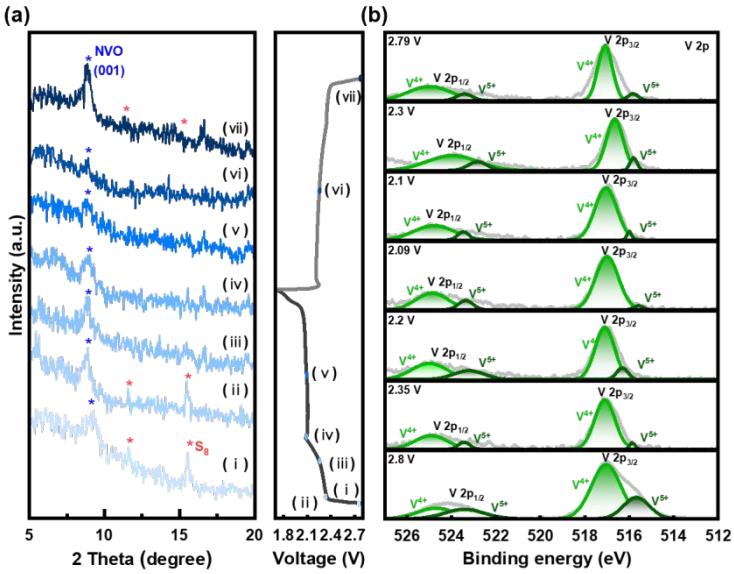

Fig. 7. (a) Ex-situ XRD patterns of NVO/AC and (b) the corresponding XPS spectra.

View Article Online
DOI: 10.1039/D6QI00145A

View Article Online
DOI: 10.1039/D6QI00145A

References

1. A. Manthiram, Y. Fu, S.-H. Chung, C. Zu and Y.-S. Su, Rechargeable Lithium–Sulfur Batteries, *Chem. Rev.*, 2014, **114**, 11751-11787.
2. S. Li and Z. Fan, Encapsulation methods of sulfur particles for lithium-sulfur batteries: A review, *Energy Storage Mater.*, 2021, **34**, 107-127.
3. J. Zhou and A. Sun, Progress in the advancement of atomically dispersed catalysts for enhanced performance lithium-sulfur batteries, *Chem. Eng. J.*, 2024, **488**, 150719.
4. R. D. Hunter, J. Ramírez-Rico and Z. Schnepp, Iron-catalyzed graphitization for the synthesis of nanostructured graphitic carbons, *J. Mater. Chem. A*, 2022, **10**, 4489-4516.
5. T. Yang, X. Tian, Y. Song, S. Wu, J. Wu and Z. Liu, Oxygen-doped carbon nanofiber nonwovens as an effective interlayer towards accelerating electrochemical kinetics for lithium-sulfur battery, *Appl. Surf. Sci.*, 2023, **611**, 155690.
6. C. Wei, Y. Han, H. Liu, R. Gan, Q. Li, Y. Wang, P. Hu, C. Ma and J. Shi, Advanced lithium–sulfur batteries enabled by a SnS_2-Hollow carbon nanofibers Flexible Electrocatalytic Membrane, *Carbon*, 2021, **184**, 1-11.
7. J. Heo, J. W. Hong, H. W. Gu, J. Sung, D. H. Kim, J. H. Kim, S. Kang, Y. J. Lee, H. Y. Choi, D. Kim, K. J. Baeg, J. T. Han and J. W. Park, A Promising Approach to Ultra-Flexible 1 Ah Lithium–Sulfur Batteries Using Oxygen-Functionalized Single-Walled Carbon Nanotubes, *Adv. Sci.*, 2024, **12**, 2406536.
8. J.-W. Park, S.-C. Jo, M.-J. Kim, I.-H. Choi, B. G. Kim, Y.-J. Lee, H.-Y. Choi, S. Kang, T. Kim and K.-J. Baeg, Flexible high-energy-density lithium-sulfur batteries using nanocarbon-embedded fibrous sulfur cathodes and membrane separators, *NPG Asia Mater.*, 2021, **13**, 30.
9. Z. Li, J. Liu, T. Wang, J. Zhu, C. Cheng, G. Ao, Z. Guan and J. Zhu, Reduced graphene oxide participation enabling fast nano-homogeneous deposition of sulfur for lithium–sulfur battery cathode, *Carbon*, 2024, **222**, 118966.
10. W. Sun, Y. Xu, X. Chen, Y. Xu, F. Wu and Y. Wang, Reduced graphene oxide modified with naphthoquinone for effective immobilization of polysulfides in high-performance Li-S

View Article Online
DOI: 10.1039/D6QI00145A

batteries, *Chem. Eng. J.*, 2020, **383**, 123111.

11. Y. Xiang, L. Lu, A. G. P. Kottapalli and Y. Pei, Status and perspectives of hierarchical porous carbon materials in terms of high-performance lithium–sulfur batteries, *Carbon Energy*, 2022, **4**, 346-398.
12. K. Zhang, Z. Hu and J. Chen, Functional porous carbon-based composite electrode materials for lithium secondary batteries, *J. Energy Chem.*, 2013, **22**, 214-225.
13. S. Waluś, G. Offer, I. Hunt, Y. Patel, T. Stockley, J. Williams and R. Purkayastha, Volumetric expansion of Lithium-Sulfur cell during operation – Fundamental insight into applicable characteristics, *Energy Storage Mater.*, 2018, **10**, 233-245.
14. A. Benítez, J. Amaro-Gahete, Y.-C. Chien, Á. Caballero, J. Morales and D. Brandell, Recent advances in lithium-sulfur batteries using biomass-derived carbons as sulfur host, *Renew. Sustain. Energy Rev.*, 2022, **154**, 111783.
15. L. Zhang, D. Liu, Z. Muhammad, F. Wan, W. Xie, Y. Wang, L. Song, Z. Niu and J. Chen, Single Nickel Atoms on Nitrogen-Doped Graphene Enabling Enhanced Kinetics of Lithium–Sulfur Batteries, *Adv. Mater.*, 2019, **31**, 1903955.
16. L. Jiao, C. Zhang, C. Geng, S. Wu, H. Li, W. Lv, Y. Tao, Z. Chen, G. Zhou, J. Li, G. Ling, Y. Wan and Q. H. Yang, Capture and Catalytic Conversion of Polysulfides by In Situ Built TiO_2-MXene Heterostructures for Lithium–Sulfur Batteries, *Adv. Energy. Mater.*, 2019, **9**, 1900219.
17. S. Rehman, T. Tang, Z. Ali, X. Huang and Y. Hou, Integrated Design of MnO_2@Carbon Hollow Nanoboxes to Synergistically Encapsulate Polysulfides for Empowering Lithium Sulfur Batteries, *Small*, 2017, **13**, 17000087.
18. L. Ni, Z. Wu, G. Zhao, C. Sun, C. Zhou, X. Gong and G. Diao, Core–Shell Structure and Interaction Mechanism of γ-MnO_2 Coated Sulfur for Improved Lithium-Sulfur Batteries, *Small*, 2017, **13**, 1603466.
19. B. Wang, R. Fang, K. Chen, S. Huang, R. Niu, Z. Yu, G. E. P. O'Connell, H. Jin, Q. Lin, J. Liang, J. M. Cairney and D. W. Wang, Heterostructured WOx/W2C Nanocatalyst for Li_2S

View Article Online
DOI: 10.1039/D6QI00145A

Oxidation in Lithium–Sulfur Batteries with High-Areal-Capacity, *Small*, 2024, **20**, 2310801.

20. R. Chen, Y. Zhou and X. Li, Fe_3C/nanocarbon-Enabled Lithium Dendrite Mitigation in Lithium–Sulfur batteries, *Small*, 2023, **20**, 2308261.

21. B. Cao, Y. Chen, D. Li, L. Yin and Y. Mo, Synthesis of TiC Nanoparticles Anchored on Hollow Carbon Nanospheres for Enhanced Polysulfide Adsorption in Li–S Batteries, *ChemSusChem*, 2016, **9**, 3338-3344.

22. Z. Sun, S. Vijay, H. H. Heenen, A. Y. S. Eng, W. Tu, Y. Zhao, S. W. Koh, P. Gao, Z. W. Seh, K. Chan and H. Li, Catalytic Polysulfide Conversion and Physiochemical Confinement for Lithium–Sulfur Batteries, *Adv. Energy. Mater.*, 2020, **10**, 1904010.

23. Z. Li, Q. He, X. Xu, Y. Zhao, X. Liu, C. Zhou, D. Ai, L. Xia and L. Mai, A 3D Nitrogen-Doped Graphene/TiN Nanowires Composite as a Strong Polysulfide Anchor for Lithium–Sulfur Batteries with Enhanced Rate Performance and High Areal Capacity, *Adv. Mater.*, 2018, **30**, 1804089.

24. J. Xu, L. Yang, S. Cao, J. Wang, Y. Ma, J. Zhang and X. Lu, Sandwiched Cathodes Assembled from CoS2-Modified Carbon Clothes for High-Performance Lithium-Sulfur Batteries, *Adv. Sci.*, 2021, **8**, 2101019.

25. Y. Zhang, Z. Mu, C. Yang, Z. Xu, S. Zhang, X. Zhang, Y. Li, J. Lai, Z. Sun, Y. Yang, Y. Chao, C. Li, X. Ge, W. Yang and S. Guo, Rational Design of MXene/1T-2H MoS_2-C Nanohybrids for High-Performance Lithium–Sulfur Batteries, *Adv. Funct. Mater.*, 2018, **28**, 1707578.

26. G. Zhou, S. Zhao, T. Wang, S.-Z. Yang, B. Johannessen, H. Chen, C. Liu, Y. Ye, Y. Wu, Y. Peng, C. Liu, S. P. Jiang, Q. Zhang and Y. Cui, Theoretical Calculation Guided Design of Single-Atom Catalysts toward Fast Kinetic and Long-Life Li–S Batteries, *Nano Lett.*, 2019, **20**, 1252-1261.

27. R. Carter, L. Oakes, N. Muralidharan, A. P. Cohn, A. Douglas and C. L. Pint, Polysulfide Anchoring Mechanism Revealed by Atomic Layer Deposition of V_2O_5 and Sulfur-Filled Carbon Nanotubes for Lithium–Sulfur Batteries, *ACS Appl. Mater. Interfaces*, 2017, **9**, 7185-7192.

View Article Online
DOI: 10.1039/D6QI00145A

28. Y. Song, W. Zhao, X. Zhu, L. Zhang, Q. Li, F. Ding, Z. Liu and J. Sun, Vanadium Dioxide-Graphene Composite with Ultrafast Anchoring Behavior of Polysulfides for Lithium–Sulfur Batteries, *ACS Appl. Mater. Interfaces*, 2018, **10**, 15733-15741.

29. Y. Wang, Y. Wang, C. Sun, Z. Han, J. Li, J. Xu, J. Qin, H. Sun and X. Wang, Multiple-Active-Site Catalysis in a Polyoxovanadate-Embedded Cobalt-Triazole Framework for Accelerated Sulfur Redox Kinetics in Lithium–Sulfur Batteries, *ACS Appl. Mater. Interfaces*, 2025, **17**, 59235-59246.

30. S. Kim, V. Soundharrajan, S. Kim, B. Sambandam, V. Mathew, J.-Y. Hwang and J. Kim, Microwave-Assisted Rapid Synthesis of $NH_4V_4O_{10}$ Layered Oxide: A High Energy Cathode for Aqueous Rechargeable Zinc Ion Batteries, *Nanomater.*, 2021, **11**, 1905.

31. Z. Feng, Y. Zhang, Y. Hao, J. Sun, C. Meng, Y. W. Zhang and J. Wang, Pulling Effects of Interlayer Water Molecules Strengthen Dry-swimming Zn^{2+} Reaction Kinetics in Layered Vanadium Oxides, *Adv. Funct. Mater.*, 2025, **35**, 2505978.

32. J. Sun, J. Yang, Y. Zhang, J. Sun, Z. Feng, T. Hu, H. Yuan, J. Liu, C. Meng, Y.-W. Zhang and J. Wang, Reduced graphene oxide pre-intercalation enables double-sided Zn^{2+} storage between VO Layers in $V_2O_5{\cdot}nH_2O$, *Energy Storage Mater.*, 2025, **83**, 104696.

33. J. Wang, Z. Ren, X. Tan, D. Chen, H. Jiang, Y. Zhang, Z. Zhou, X. Zhu and C. Meng, Boosting ammonium-ion storage of $V_2O_5{\cdot}nH_2O$ by encapsulating engineering of polyaniline, *J. Colloid Interface Sci.*, 2025, **692**, 137482.

34. W. Li, H. Li, H. Chen, F. Sun and G. Li, Vanadium-Based Sulfur Electrocatalysts for High-Performance Lithium-Sulfur Batteries, *Chem.*, 2026, e03601.

35. X. Chen, X. Chen, Y. Wang, D. Qi, J. H. Liu, Y. Huang, H. Jiang, P. Yan, X. Jiang and D. Cao, Interfacial Orbital Hybridization in Multiphase Mn-V Oxide Enabling Long-Life and High-Power Aqueous Zinc-Ion Batteries, *Adv. Funct. Mater.*, 2026, e28874.

36. X. Chen, X. Chen, X. Lin, D. Qi, J.-H. Liu, Y. Huang, C. Zhan, H. Zhang, Y. Gao and Y. Xiao, Suppressing Jahn-Teller distortion and accelerating ion kinetics via heterostructure engineering for stable aqueous zinc-ion batteries, *Chem. Eng. J.*, 2025, **526**, 170760.

View Article Online
DOI: 10.1039/D6QI00145A

37. Y. Chen, X. Hu, X. Chen, J.-H. Liu, Y. Huang and D. Cao, Trimetallic-Organic Framework-Derived Ni-Doped MnO/PC as cathodes for High-Performance aqueous zinc-ion batteries, *Chem. Eng. J.*, 2023, **478**, 147411.

38. H. Jiang, J. Fu, Y. Wang, X. Jiang, P. Yan, J.-H. Liu, C. Zhan, X. Cao and X. Chen, Hierarchical V_2O_5 cathode derived from π-conjugated thiophene metal-organic framework enabling ultra-stable and high-rate aqueous zinc-ion storage, *J. Energy. Storage*, 2026, **150**, 120452.

39. X. Hu, X. Chen, Y. Chen, Z. Li, Y. Huang, L. Deng and D. Cao, Synergistic H^+/Zn^{2+} co-insertion mechanism in vanadium trioxide composited on carbon nanotubes cathode for aqueous zinc ion batteries, *J. Alloys Compd.*, 2023, **945**, 169271.

40. X. Chen, X. Hu, Y. Chen, X. Cao, Y. Huang, H. Zhang, J.-H. Liu, Y. Wang, S.-L. Chou and D. Cao, Ultrastable hydrated vanadium dioxide cathodes for high-performance aqueous zinc ion batteries with H^+/Zn^{2+} Co-insertion mechanism, *J. Mater. Chem. A*, 2022, **10**, 22194-22204.

41. Y. Wang, Y. Fan, X. Chen, J. H. Liu, Y. Gao, X. Lin, Y. Huang, H. Jiang, C. Zhan, H. Zhang, X. Cao and Y. Xiao, Synergistic Effects of Structural and Electronic Dual Engineering for Ultra-Stable Aqueous Zinc-Ion Batteries, *InfoMat*, 2025, **7**, e70055.

42. G. Kresse and J. Furthmüller, Efficient iterative schemes for ab initio total-energy calculations using a plane-wave basis set, *Physical Review B*, 1996, **54**, 11169-11186.

43. J. P. Perdew, K. Burke and M. Ernzerhof, Generalized Gradient Approximation Made Simple, *Phys. Rev. Lett.*, 1996, **77**, 3865-3868.

44. P. E. Blöchl, Projector augmented-wave method, *Physical Review B*, 1994, **50**, 17953-17979.

45. S. Yao and Y. Sun, Defect engineering and morphology adjustment assist $NH_4V_4O_{10}$ to be a high-performance aqueous zinc ion battery cathode, *J. Mater. Chem. A*, 2024, **12**, 17213-17221.

46. L. Pan, Y. Sun, S. Yao, Y. Zhang and Z. Wen, Stable structure and oxygen-rich vacancy assist $NH_4V_4O_{10}$ to become a high-performance aqueous zinc-ion battery cathode material, *J. Alloys Compd.*, 2025, **1010**, 177949.

47. R. Ojha, S. Maniam, S. M. R. Niya, A. S. Rigoni, K. Tran, A. Tanksale, M. J. S. Spencer and J. Andrews, Insights into the structure-property relationships of activated carbon derived from

View Article Online
DOI: 10.1039/D6QI00145A

phenolic resin for electrochemical storage of green hydrogen using proton battery, *J. Energy. Storage*, 2025, **107**, 114912.

48. Z. Li, L. Deng, I. A. Kinloch and R. J. Young, Raman spectroscopy of carbon materials and their composites: Graphene, nanotubes and fibres, *Prog. Mater Sci.*, 2023, **135**, 101089.

49. Z. Wang, H. Wang, X. Bai, J. Dong, K. Zhang, K. Zhan and B. Zhao, Pre-Intercalation of Metal Ions into Ammonium Vanadate Nanostructures toward Advanced Zinc Ion Batteries, *ACS Appl. Nano Mater.*, 2024, **7**, 27090-27099.

50. P. Shvets, O. Dikaya, K. Maksimova and A. Goikhman, A review of Raman spectroscopy of vanadium oxides, *J. Raman Spectrosc.*, 2019, **50**, 1226-1244.

51. W. Chen, L. Mai, J. Peng, Q. Xu and Q. Zhu, Raman spectroscopic study of vanadium oxide nanotubes, *J. Solid State Chem.*, 2004, **177**, 377-379.

52. F. D. Hardcastlet and I. E. Wachs, Determlnation of Vanadium-Oxygen Bond Distances and Bond Orders by Raman Spectroscopy, *J. Phys. Chem.*, 1991, **95**, 5031.

53. Q. Li, X. Rui, D. Chen, Y. Feng, N. Xiao, L. Gan, Q. Zhang, Y. Yu and S. Huang, A High-Capacity Ammonium Vanadate Cathode for Zinc-Ion Battery, *Nanomicro Lett*, 2020, **12**, 67.

54. Y. Liu, X. Xu, M. Sadd, O. O. Kapitanova, V. A. Krivchenko, J. Ban, J. Wang, X. Jiao, Z. Song, J. Song, S. Xiong and A. Matic, Insight into the Critical Role of Exchange Current Density on Electrodeposition Behavior of Lithium Metal, *Adv. Sci.*, 2021, **8**, 2003301.

55. Z. Li, Y. Zhou, Y. Wang and Y. C. Lu, Solvent-Mediated Li_2S Electrodeposition: A Critical Manipulator in Lithium–Sulfur Batteries, *Adv. Energy. Mater.*, 2018, **9**, 1802207.

56. D.-Q. Cai, J.-L. Yang, T. Liu, S.-X. Zhao and G. Cao, Interfaces-dominated Li_2S nucleation behavior enabled by heterostructure catalyst for fast kinetics Li-S batteries, *Nano Energy*, 2021, **89**.

57. J. Sun, Y. Liu, L. Liu, J. Bi, S. Wang, Z. Du, H. Du, K. Wang, W. Ai and W. Huang, Interface Engineering Toward Expedited Li(2) S Deposition in Lithium-Sulfur Batteries: A Critical Review, *Adv. Mater.*, 2023, **35**, e2211168.

58. Y. Wang, Y. Wei, B. Wang, P. Jing, Y. Zhang, Y. Zhang, Q. Wang and H. Wu, Bio-assisted

View Article Online
DOI: 10.1039/D6QI00145A

engineering of hierarchical porous carbon nanofiber host in-situ embedded with iron carbide nanocatalysts toward high-performance Li–S batteries, *Carbon*, 2021, **177**, 60-70.

59. Y. Yang, X. Li, R. Luo, X. Zhang, J. Fu, Y. Zheng, K. Huo and T. Zhou, A topochemically constructed flexible heterogeneous vanadium-based electrocatalyst for boosted conversion kinetics of polysulfides in Li–S batteries, *Mater. Chem. Front.*, 2021, **5**, 3830-3840.

60. D. Yang, Z. Liang, C. Zhang, J. J. Biendicho, M. Botifoll, M. C. Spadaro, Q. Chen, M. Li, A. Ramon, A. O. Moghaddam, J. Llorca, J. Wang, J. R. Morante, J. Arbiol, S. L. Chou and A. Cabot, $NbSe_2$ Meets C_2N: A 2D-2D Heterostructure Catalysts as Multifunctional Polysulfide Mediator in Ultra-Long-Life Lithium–Sulfur Batteries, *Adv. Energy. Mater.*, 2021, **11**, 2101250.

61. J. Ren and Q. Zhao, Preparation of a lithium–sulfur battery diaphragm catalyst and its battery performance, *RSC Adv.*, 2024, **14**, 36471-36487.

62. X. Dai, G. Lv, Z. Wu, X. Wang, Y. Liu, J. Sun, Q. Wang, X. Xiong, Y. Liu, C. Zhang, S. Xin, Y. Chen and T. Zhou, Flexible Hierarchical Co-Doped NiS_2@CNF-CNT Electron Deficient Interlayer with Grass-Roots Structure for Li–S Batteries, *Adv. Energy. Mater.*, 2023, **13**, 2300452.

View Article Online
DOI: 10.1039/D6QI00145A

Data Availability Statement

The following data supporting this article have been included as part of the Supplementary Information (SI): SEM, surface model used in the DFT calculation, differential charge density plots, CV peak current relationship, GITT, EIS Nyquist plots, comparative Q_H and Q_L values, plots of dQ/dV versus V, voltage profiles at the 10^{th} and 100^{th} cycles (0.5 C).